Nano Today 52 (2023) 101968

Contents lists available at ScienceDirect

Nano Today

journal homepage: www.elsevier.com/locate/nanotoday

DeepGT: Deep learning-based quantification of nanosized bioparticles in bright-field micrographs of Gires-Tournois biosensor

Jiwon Kang [a,1], Young Jin Yoo [a,b,1], Jin-Hwi Park [c,1], Joo Hwan Ko [a], Seungtaek Kim [d], Stefan G. Stanciu [e], Harald A. Stenmark [f], JinAh Lee [d], Abdullah Al Mahmud [a], Hae-Gon Jeon [c,*], Young Min Song [a,c,g,**]

[a] School of Electrical Engineering and Computer Science, Gwangju Institute of Science and Technology, Gwangju 61005, Republic of Korea
[b] Department of Mechanical Engineering, Massachusetts Institute of Technology, Cambridge, MA 02139, USA
[c] AI Graduate School, Gwangju Institute of Science and Technology, Gwangju 61005, Republic of Korea
[d] Zoonotic Virus Laboratory, Institut Pasteur Korea, Seongnam 13488, Republic of Korea
[e] Center for Microscopy-Microanalysis and Information Processing, Politehnica University of Bucharest, 060042 Bucharest, Romania
[f] Department of Molecular Cell Biology, Institute for Cancer Research, Oslo University Hospital, 0379 Oslo, Norway
[g] Anti-Viral Research Center, Gwangju Institute of Science and Technology, Gwangju 61005, Republic of Korea

ARTICLE INFO

Keywords:
Quantitative biosensing
Gires-Tournois biosensor
Deep learning
Nanosized bioparticles
Bright-field microscopy

ABSTRACT

Rapid and decentralized quantification of viral load profiles in infected patients is vital for assessing clinical severity and tailoring appropriate therapeutic strategies. Although microscopic imaging offers potential for label-free and amplification-free quantitative diagnostics, the small size (~100 nm in diameter) and low refractive index (n ~1.5) of bioparticles present challenges in achieving accurate estimations, consequently increasing the limit of detection (LoD). In this study, we present a novel synergistic biosensing approach, DeepGT, combining Gires-Tournois (GT) sensing platforms with deep learning algorithms to enhance nanoscale bioparticle counting accuracy. The GT sensing platform serves as a photonic resonator, increasing bioparticle visibility in bright-field microscopy and maximizing chromatic contrast. By employing a back-end with a dilated convolutional neural network architecture, DeepGT effectively refines artifacts and color deviations, significantly improving particle estimation accuracy (MAE ~2.37 across 1596 images) compared to rule-based algorithms (MAE ~ 13.47). Notably, the enhanced accuracy in detecting invisible particles (e.g., two- or three-particles) enables an LoD of 138 pg ml^{-1}, facilitating a dynamic linear correlation at low viral concentration ranges within the clinical spectrum of infection, from asymptomatic to severe cases. Leveraging transfer learning, DeepGT, which relies on a chromatometry-based strategy instead of a spatial resolution approach, exhibits exceptional precision when analyzing particles of diverse dimensions smaller than the microscopy system's minimum diffraction limit in visible light (< 258 nm). The DeepGT approach holds promise for early screening and triage of emerging viruses, reducing costs and time requirements in diagnostics.

Introduction

Ubiquitous and rapid diagnostic tests can identify new infection cases on-site and facilitate the immediate treatment and/or isolation of infected individuals, to prevent the further spread of viruses [1–3]. Disease outbreaks such as the COVID-19 pandemic have emphasized the deficiencies of centralized laboratory diagnostic systems and the lengthy periods of time they require to process samples and provide results [3,4]. Furthermore, prolonged qualitative diagnosis has led to either under-medication/treatment or conversely over-medication/isolation of infected patients [1,5]. Recent clinical studies have suggested a strong association between viral load and clinical severity [2,6–11], which underlines viral load as a potentially highly predictive risk factor for severe viral infections and a crucial marker for designing optimal

* Correspondence to: AI Graduate School, Gwangju Institute of Science and Technology, 123, Cheomdangwagi-ro, Buk-gu, Gwangju 61005, Republic of Korea.
** Correspondence to: School of Electrical Engineering and Computer Science, Gwangju Institute of Science and Technology, 123, Cheomdangwagi-ro, Buk-gu, Gwangju 61005, Republic of Korea.
E-mail addresses: haegonj@gist.ac.kr (H.-G. Jeon), ymsong@gist.ac.kr (Y.M. Song).
[1] These authors contributed equally.

https://doi.org/10.1016/j.nantod.2023.101968
Received 8 April 2023; Received in revised form 24 July 2023; Accepted 13 August 2023
Available online 24 August 2023

clinical interventions. Quantitative laboratory-based testing [e.g., quantitative polymerase chain reaction (qPCR) [12,13] is labor intensive, requiring specialized facilities with skilled staff and specific infrastructures for various tasks (e.g., sample processing, nucleic acid extraction, thermocycling, and data analysis). Moreover, the complexity of sample preparation, including fluorophore labeling and/or amplification, can significantly impact both the turnaround time and accuracy of testing, as it has the potential to amplify unintended nucleic acid sequences [14,15]. Alternatively, the development of automated rapid/quantitative diagnostic technologies based on intuitive/inexpensive test kits offers opportunities to diagnose patients immediately at the point-of-care and provide appropriate treatment options for clinical severity commensurate with quantitative loads [8,10,11].

Viruses are typically smaller than the diffraction limit (< 258 nm; see Methods for a detailed formula) of a typical bright-field microscopy system and have a low refractive index ($n \sim 1.5$) [16,17], inducing weak light-matter interactions. Accurately quantifying viruses smaller than the wavelength of visible rays (400–800 nm) presents a significant challenge due to the ambiguous and blurred images obtained from a typical upright microscope, further complicated by the similarity in refractive index between biological nanoparticles and the sliding glasses in a conventional microscope. Various imaging modalities have been developed to achieve high resolution and accurate quantitation of biological tissues; these include confocal microscopy [18], two-photon fluorescence [19], second harmonic generation [20], Raman spectroscopy [21], Fourier-transform microscopy [22], and electron microscopy [23]. Although these techniques have been successful in advancing biomedical research, their use is limited owing to the requirement for sophisticated equipment and professional expertise. Recently, advanced nanophotonic technologies have been developed using plasmonic-based nanostructures, primarily for microscale cell-imaging applications (e.g., colorimetric histology [24,25] and ptychographic phase microscopy [26]). Nanophotonic biosensors based on surface-enhanced Raman scattering [27] and surface plasmon resonance [28], have been studied for targeting nanoparticles, but still suffer from noise, reproducibility, uniformity, and rapid imaging challenges [29,30]. To alleviate these drawbacks and to provide a holistic approach to complex data [31], machine learning has been applied to conventional nanophotonic biosensors. The remarkable ability of artificial intelligence models based on deep convolutional neural networks (CNNs) to process vast amounts of data and extract subtle information, sometimes unavailable to human experts, has played a pivotal role in many fields. In particular, computer vision [32,33] using CNNs has demonstrated superior object categorization skills similar to human vision [34] and has been successfully applied to various biomedical applications (e.g., protein structure prediction [35] and cell counting [36–38]).

In our previous studies [39,40], the tunable trilayered Gires-Tournois (GT) immunosensor, which is a nanophotonic resonator, was designed to interact with minuscule biological analytes and to produce colorful micrographs based on chromatometry for specific analyte loads through a bright-field microscope without any additional accessories. Despite the advantage of not requiring nanopatterning or synthesis, several visual artifacts emerged during the process (e.g., surface defects, impurities, and salts), resulting in inherent issues such as non-uniformity and non-reproducibility. Therefore, conventional chromatic analysis was not able to reliably distinguish between normal bioparticles and visual artifacts (displaying a similar color to the normal bioparticles), thereby leading to a limit of quantification that was not consistently close to that of qPCR. Even though supervised deep learning (DL) has the potential to exceed conventional approaches and provides effective performance, the need for well-curated and ground truth-tagged training datasets remains a hurdle for conventional labs in terms of cost, time, and labor [31,41].

Here, we present an intuitive biosensing framework, named DeepGT, that is highly efficient in quantifying nanoscale bioparticles using nanophotonics and DL without the need for any sample preparation or parameter fitting. The GT biosensors composed of trilayered thin films and a biofunctionalized surface, designed to target specific analytes are used to directly facilitate dynamic colorimetric sensing. The functionality of the GT biosensor was successfully verified through the utilization of synthesized virus-like particles. These particles were created by combining SARS-CoV-2 antigens with SiO_2 nanospheres, effectively simulating the binding mechanism between the virus and host cells. After detecting bioparticles mimicking the SARS-CoV-2 using the GT biosensors functionalized with SARS-CoV-2 antibodies, we obtained images of diverse structures of nanoparticle (NP) clusters mounted on the GT biosensors through a conventional bright-field optical microscope (OM) and scanning electron microscope (SEM), and subsequently annotated 2336 image pairs (1596 image pairs for training main model and the others for hard negative sampling and transfer learning). Considering the limited quantity of training data for Big Data applications, we employed data augmentation and five-fold cross-validation to address the training set's scarcity and boost the performance of CNNs. The optimized DeepGT, trained with ground truth density maps derived from SEM images and supplemented with hard negative samples containing diverse visual artifacts, was applied to infer the effective count of NPs in OM images. DeepGT filtered out irrelevant information and extracted only the desired data, leading to a comparable detection limit of 138 pg ml^{-1} to existing diagnostics [6] and ensuring a dynamic linear correlation at low viral concentration range from 'asymptomatic' to 'severe' [7,42,43]. Furthermore, we utilized the pre-trained DeepGT to measure analytes across a broad size spectrum, encompassing zoonotic animal viruses, by implementing transfer learning, which resulted in remarkable transferability with limited datasets [44,45].

Results

Visualization and quantification of nanoscale bioparticles using nanophotonics and DL

Fig. 1 illustrates the visualization and quantification of nanoscale bioparticles using nanophotonics and DL. We employed a planar photonic resonator in a trilayered thin-film configuration without sophisticated geometries [39,40]. This configuration can produce a strong resonance without requiring nanopatterning, and it can be readily manufactured on a large scale (Fig. 1a). The proposed thin-film structure features a porous (P_r) lossy layer on a metal substrate; this acts as a GT resonator with a strong/sensitive resonance, providing distinct detection and design flexibility for diverse analytes. For the optical modeling of the GT resonator, we used the minima reflectance solver. This was based on impedance matching and finite-difference time-domain (FDTD) calculations. This was done for a near-unity absorption condition at a visible wavelength of 528 nm in the range of chromatic sensitivity (Supplementary Fig. S1). The refractive indices of the oxide and lossy layers were considered based on the refractive index of the target analyte (Fig. 1b and Supplementary Fig. S2). After solving for the minima reflectance conditions, the fabrication parameters were derived by considering realistic modeling conditions from the various solutions for unity absorption. Taking the optimal parameters (t_{oxide}, t_{lossy}, and P_r), we fabricated oxide and lossy layers using plasma-enhanced chemical vapor deposition (PECVD) and electron-beam physical vapor deposition (EBPVD), respectively (see Methods for a detailed description; Fig. 1c and Supplementary Fig. S3). The optimized resonator was then functionalized with an antibody that selectively reacted to a specific antigen to utilize as biosensors (see Methods for a detailed description; Supplementary Fig. S4). In the biosensing procedure, NP agglomerations are induced by the hydrodynamic phenomenon of evaporation, specifically through Marangoni flow, which is influenced by temperature and humidity [46]. We subjected the surface to plasma treatment for achieving hydrophilicity to ensure maximum evaporation and consistent drying sequences regardless of temperature and humidity conditions. Sequentially, we carefully dispensed a minimal volume of solution (300 nl)

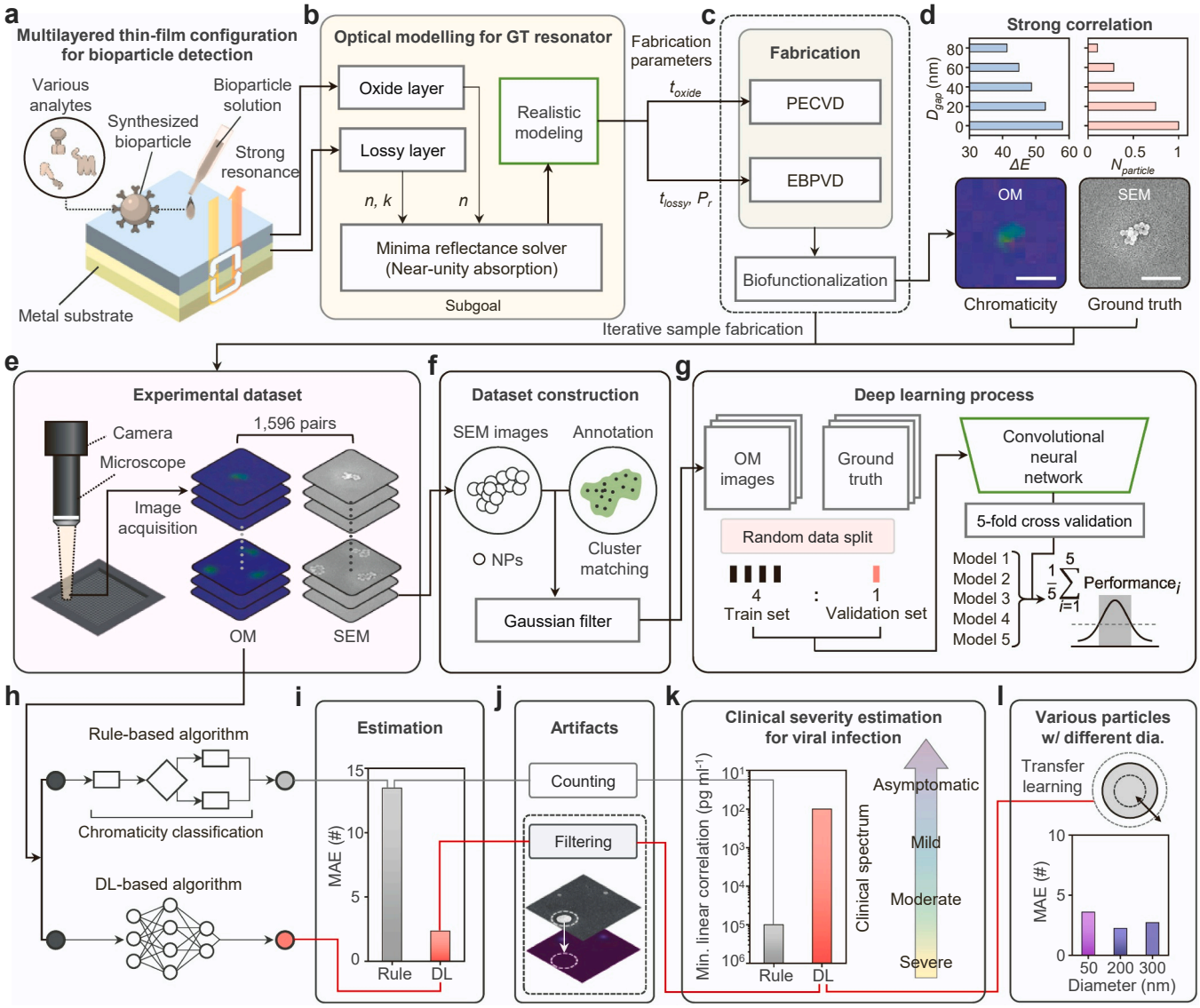

Fig. 1. Quantitative bright-field imaging of nanoscale bioparticles based on multilayered thin-film via deep learning. (a) Multilayered thin-film resonator, to produce a strong resonance between the bioparticles of various analytes. (b) Optical modeling for the oxide layer and lossy layer, to achieve near-unity absorption and derive the fabrication parameters for realistic modeling; *n*, refractive index; *k*, extinction coefficient; t_{oxide}, thickness of oxide material; t_{lossy}, thickness of lossy layer; P_r, porosity of lossy media. (c) Fabrication using PECVD and EBPVD (depending on fabrication parameters) followed by biofunctionalization to produce an immunosensor. *PECVD*, plasma enhanced chemical vapor deposition; *EBPVD*, electron-beam physical vapor deposition. (d) Strong linear correlation between chromaticity and ground truth number of nanosized bioparticles in OM and SEM images; D_{gap}, the gap distance between particles; *ΔE*, color difference; $N_{particle}$, effective number of bioparticles; *OM*, optical microscopy; *SEM*, scanning electron microscopy. (e) Iterative sample fabrication for obtaining an experimental dataset of 1596 pairs of OM and SEM images. (f) Annotating the SEM images and blurring via the Gaussian filter for ground truthing; *NPs*, nanoparticles. (g) OM images and ground truth density maps; these were split (to perform five-fold cross-validation of the CNN) and then their performances were averaged over to establish a robust main DL model; *CNN*, convolutional neural network; *DL*, deep learning. (h) Illustrations of the rule-based algorithm according to chromaticity classification and DL-based CNN algorithm for analyzing OM images. (i) DeepGT showing a lower MAE than the rule-based one. (j) Artifacts, which are counted in the rule-based analysis but filtered in DeepGT. (k) Clinical severity, which can be estimated from the analysis algorithm for viral infection within the minimum linear correlation range. (l) Transfer learning for various particles with different diameters; *dia*, diameter. Scale bar: 1 μm. The raw SEM and OM images dataset and the annotations are available on the Figshare repository at https://doi.org/10.6084/m9.figshare.c.6468460.v1.

containing NPs onto the biofunctionalized surface of the GT biosensor [47]. The bioparticles adsorbed on the surface of the fabricated structure formed clusters (within the desired concentration range) which were chromatically distinguishable in OM images. Optical simulation results revealed a strong linear correlation between chromaticity and particle distribution based on the gap distance between particles (D_{gap}). This was supported by the comparison of bright-field micrographs and their corresponding scanning electron microscopy (SEM) images (Fig. 1d and Supplementary Fig. S5). We could use this for quantitative analysis.

For the experimental dataset, multiple images were acquired from iteratively fabricated samples using a camera-equipped microscope; these were then matched with the corresponding SEM images (Fig. 1e and Supplementary Figs. S6 and S7. All data are available on the Figshare repository at https://doi.org/10.6084/m9.figshare.c.6468460.v1). For the DL process, ground truths were constructed via cluster-matching-based annotation of the SEM images in the acquired dataset, assisted by Gaussian filtering (Fig. 1f). Prior to the DL process, the training and validation sets were grouped via random data-splitting, for efficient dataset utilization of the OM images and ground truths. For chromatic analysis, we utilized a CNN that shows strong performance in

visual image analysis as a feature extractor of color images, and performed five-fold cross-validation to improve the accuracy of analysis, resulting in the establishment of DeepGT (Fig. 1g).

After learning, we evaluated the accuracy improvement by comparing DeepGT against a conventional rule-based algorithm [39] that classified a limited range of chromaticity values (Fig. 1h). The particle estimation results show that DeepGT yielded five-fold lower value compared to the rule-based algorithm in terms of mean absolute error (MAE), because optimized neural networks can refine the irrelevant information (Fig. 1i). Moreover, DeepGT can automatically refine various visual artifacts that might adversely affect evaluation [48]. In contrast, rule-based algorithms do not filter out these artifacts. Instead, they count them as analytes (Fig. 1j). A dynamic linear correlation for bioparticle quantification in a lower concentration range facilitates clinical spectrum diagnosis via detailed clinical severity estimation grades for viral infection (Fig. 1k). Unlike rule-based algorithms, DeepGT can easily build evaluation models and achieve low MAEs for particles of different sizes, via transfer learning (Fig. 1l).

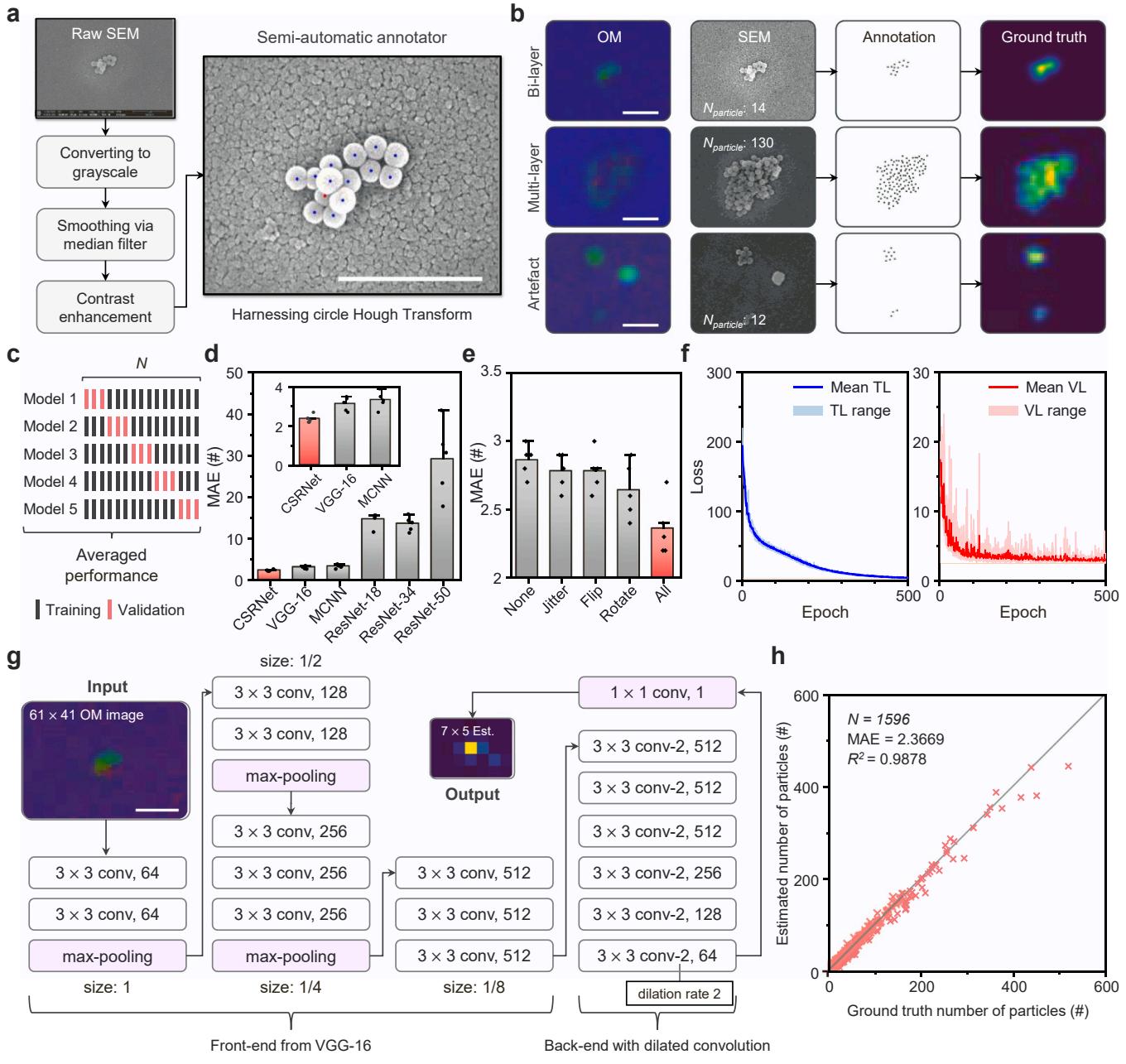

Fig. 2. Dataset construction and optimization for deep learning and inference results. (a) cHT-based semi-automatic annotator, used for constructing ground truth data from raw SEM images; *cHT*, circle Hough Transform. (b) Representative OM, SEM images, annotations, and ground truth density maps of the dataset ($N = 1596$). (c) Schematic illustration of the five-fold cross-validation. (d) MAEs of different deep neural networks; Inset: enlarged bar charts; *MAE*, mean absolute error; *MCNN*, multi-column convolutional neural network. (e) MAEs of augmentation methods. (f) Training loss and validation loss range of the five-fold cross-validation and their mean values. (g) Architecture of the CSRNet, which converges OM images (61 × 41 pixels) to estimated density map (7 × 5 pixels); *conv*, convolution; *conv-2*, convolution with a dilation rate of 2; *Est.*, estimation. (h) Scatter plots of ground truth vs. estimation using a CSRNet; R^2, coefficient of determination. All scale bars: 1 μm. See Supplementary Movie S1 and Supplementary Fig. S8 for the annotating procedure in (a). The raw SEM and OM images dataset and the annotations are available on the Figshare repository at https://doi.org/10.6084/m9.figshare.c.6468460.v1.

Dataset construction and effective number of particle estimations using CNN

Fig. 2a shows the image processing steps (including grayscale conversion, filtering, and contrast enhancement) applied to the raw SEM images for labeling via annotator and digitization of the captured NP positions (see also Supplementary Fig. S8 for the detailed sequence). The overlaid particles and visual artifacts were accurately annotated to construct the well-curated dataset, thereby training a robust DL model. By employing a semi-automatic annotator based on the circle Hough Transform, we minimized the human error and edited the NP labels using five tunable parameters: diameter, eccentricity, and three tolerancing conditions of particles (Supplementary Video S1). The discretely dotted annotations were successively spread by a Gaussian filter to preserve the continuous spatial distribution and to construct the ground truth density map (see Methods for details; Fig. 2b). A comparative analysis was performed to determine the optimal spreading filter from among six candidates (Supplementary Fig. S9). Consequently, the Gaussian spread function, in which profile approximates the Airy disk [49] as the pattern of far-field diffraction, was selected for transforming the ground truth density map. The optimal standard deviation of the Gaussian filter was determined to be 1 (from a range of 0.1–5) to closely match the cluster area of the OM image (Supplementary Fig. S10). Hard negative data by visual artifacts (i.e., a ground truth value of zero) were ignored in annotation, to facilitate the precise auto-filtering process. The clusters adsorbed onto the GT biosensor were also classified according to three criteria: the number of particles, clusters, and layers (Supplementary Fig. S11).

To enhance the accuracy of particle count estimation for the OM images, we adopted five-fold cross-validation [50,51], which reduces overfitting and provides more accurate performance estimates for limited datasets. The overall average performances of the five DL models were evaluated after training using 80% of the dataset and validated using the remaining 20% via five-fold cross-validation (Fig. 2c). To adopt the most suitable model for maximizing prediction performance, we compared six neural networks widely used for crowd counting: CSRNet [52], VGG-16 [53], MCNN [54], and ResNet-50 [55]. Among these, CSRNet achieved the lowest MAE in prediction (Fig. 2d and Supplementary Fig. S12). The efficient architecture of CSRNet, with ten times fewer parameters than VGG-16 as the second-lowest MAE, requires an assay time of ~3 ms (see Methods for detailed training equipment). Considering the difficulties associated with generating large-scale ground truth datasets for DeepGT, several data augmentation techniques [56] (i.e., jittering, flipping, and rotation) were conducted to enrich the existing dataset (Supplementary Fig. S13). Rotation and flipping were randomly applied to the OM images allowing the DL model to learn diverse cluster shapes, and jittering was used to modify the brightness, saturation, and color contrast of pixel information within an appropriate range (for an ablation study for data augmentation, see Supplementary Table S1). These three methods reduced the MAEs to 2.78, 2.78, and 2.64, respectively, compared to the initial value of 2.86, and applying all three of them simultaneously resulted in the lowest value of 2.37 (Fig. 2e). The training loss (TL) and validation loss (VL) during the five-fold cross-validation process for CSRNet showed that neither overfitting nor underfitting occurred (Fig. 2f and Supplementary Fig. S14).

Fig. 2g illustrates the architecture of CSRNet, which consists of a front-end and a back-end for generating density maps, in contrast to other CNN-based density estimations [57–59]. The front-end consists of convolutional layers from VGG-16, which possesses strong transfer learning capabilities and can be adapted to facilitate integration with the back-end. The front-end, which includes three max-pooling layers, produces an output density map of 7 × 5 pixels, which was reduced to 1/8 of the original input OM image size (61 × 41 pixels) (Supplementary Fig. S15). The back-end of the CSRNet uses dilated convolutional layers with dilation rates of two to aggregate the multiscale contextual information (for an ablation study for dilation rate, see Supplementary Table S2). Dilated convolution exploits sparse kernels to enlarge the receptive field of a network without increasing the number of additional layers or parameters. By adding gaps between the pixels in the convolutional kernel, and effectively skipping several pixels, the receptive field can be expanded beyond the size of the kernel, allowing the network to capture a more extensive context without increasing the number of parameters or the computational complexity. Because nanosized bioparticle images have highly ambiguous and complex configurations, the dilated convolution filter preserves the contextual information of the NPs. Based on this architecture, we finally achieved an MAE of 2.3669 by comparing the particle count obtained from the estimated density map with the ground truth particle count for 1596 images (Fig. 2h). Our empirical analysis suggests that adding more convolutional and pooling layers can decrease the output size and hinder the generation of high-quality density maps. Thus, our architectural setup is optimal for learning nanoscale bioparticles from limited data, while also preventing overfitting and underfitting. The coefficient of determination (R^2) of 0.9878 indicates that the trained DeepGT can accurately predict the number of particles without any bias.

Linear quantification for low virus concentration using refined information

Evaluating viral concentration using a single viral cluster presents challenges in practical biosensing scenarios. To overcome this, we decided to define a wider sensing area of 1 mm × 1 mm in size and aggregate the particle count across the entire area. After the biosensing process, the defined sensing area (filled with NPs in proportion to the concentration of the viral solution) was raster-scanned with the OM to construct a high-magnified stitched image for DeepGT quantification (Supplementary Fig. S16). Diverse structures of NP agglomerations (including imperceptible particles and complex forms), along with some inevitable visual artifacts, were produced during the entire process including the vapor deposition and biosensing. To achieve precise quantitative biosensing, the elimination of irrelevant information from the raw OM images and real-time counting of refined information are necessary. Due to the relatively insignificant colors of NP clusters consisting of two or three particles in the OM images, the rule-based algorithm based on chromatic analysis identifies these cases as imperceptible particles. In contrast, DeepGT accurately extracts features of these imperceptible particles and infers their presence with high accuracy (Fig. 3a). While the rule-based algorithm was unable to detect the two-particle clusters at all, DeepGT was able to recognize their existence using trained features (Fig. 3b). For the three-particle clusters, the rule-based algorithm provided an estimate with a mean value of 0.48 and a standard deviation (*SD*) of 1.35; however, DeepGT accurately inferred with a mean value of 3.58 and an *SD* of 0.57. Fig. 3c presents scatter plots for comparing DeepGT and rule-based analysis of artifact-encompassed images. Using the rule-based algorithm, clusters composed of less than twenty NPs were undercounted (gray crosses beneath the diagonal line); in contrast, dense scattered red dots representing DeepGT near the diagonal line indicated accurate and unbiased inference.

Notably, DeepGT extracts the features of NP clusters in the OM images without relying on seeming color, which can be confusing for the rule-based algorithm (see Supplementary Table S3 comparing DeepGT with the rule-based approach). The rule-based algorithm overcounts most artifact-encompassed images due to the visual artifacts (displaying a similar hue to the NP clusters) (Fig. 3d). DeepGT was trained with 139 additional hard negative images (with a ground truth value of zero), comprising 50, 50, and 39 images of large defects, small defects, and impurities, respectively, to mitigate the risk of misreading (Supplementary Fig. S17). The automated identification and filtering of artifacts resulted in a decrease in the estimated number of NPs in an image containing an artifact to 11.7, which is approximately the ground truth value of 15. In addition, multi-layer regions (i.e., those comprising more

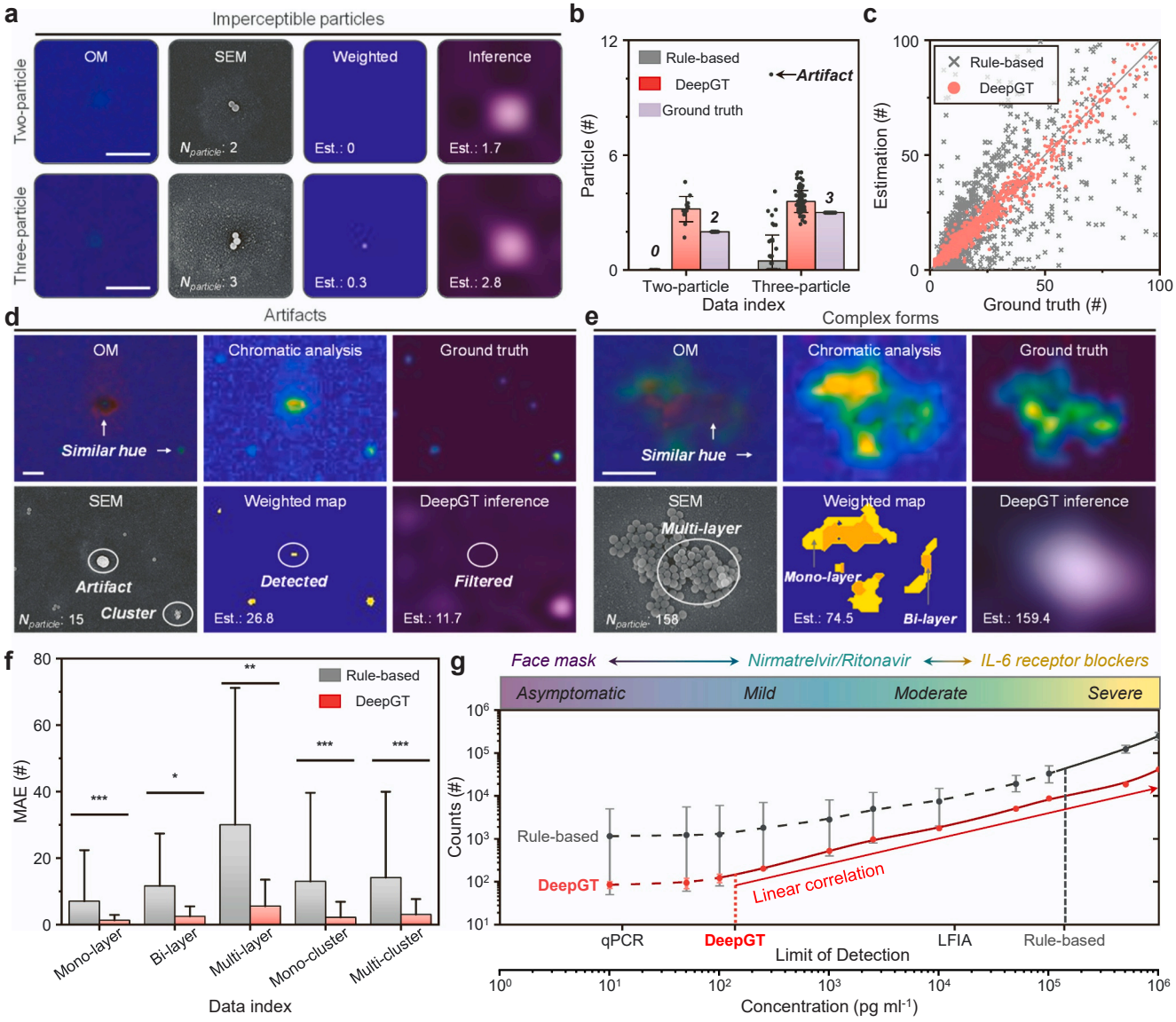

Fig. 3. Reported case within the sensing area and linear quantification for low virus concentration. (a) Comparison between rule-based algorithm and DeepGT for imperceptible particles: two-particle (top) and three-particle clusters (bottom). (b) Bar charts of estimation and ground truth number for imperceptible particles. (c) Scatter plots of ground truth vs. estimation using a rule-based algorithm (gray crosses) and DeepGT (red circles). (d-e) Comparison between rule-based analysis and DeepGT (d) for the artifact-encompassed image and (e) for the complex-form-encompassed image. (f) Bar charts of the mean and *SD* of absolute error depending on the data indices and approaches. Data displayed as the mean + *SD*. * $P < 0.1$, ** $P < 0.01$, *** $P < 0.001$ via one-way ANOVA; *SD*, standard deviation. (g) Comparison of the limit of detection for virus analyses and linear correlation range of the DeepGT. Top marker denotes severity and interventions with respect to the viral concentration; *qPCR*, quantitative polymerase chain reaction; *LFIA*, lateral-flow immunoassay; *IL-6*, interleukin-6. The gray and red graphical data in (b), (c), (f), and (g) show experimental results obtained from rule-based analysis and DeepGT, respectively. In the plots shown in (g), the dots denote the median value, and the starts and ends of the horizontal lines denote the minimum and maximum values, respectively. All scale bars: 1 μm. The raw SEM and OM images dataset and the annotations are available on the Figshare repository at https://doi.org/10.6084/m9.figshare.c.6468460.v1.

than three layers of NPs; displaying a similar hue to the background) in the multi-layer clusters also misinform the chromatic classifier of the rule-based algorithm, resulting in a significant undercount (Fig. 3e). However, the automatically generated DL model in DeepGT exactly infers the existence of multi-layer NPs by featuring contexts, resulting in an estimation of 159.4, which is approximately the ground truth value of 158.

The refinement of artifacts and accurate quantification of imperceptible particles and complex forms significantly reduce the MAEs of the overall data indices across the 1596 dataset, especially in multi-layer clusters, which decreased from 30.0 to 5.56 (Fig. 3f). Thus, DeepGT demonstrates a more accurate and robust performance without noticeable outliers. Fig. 3g shows a linear correlation between the viral concentration and sensing particle count produced via DeepGT and rule-based analysis. Even at low virus concentrations, DeepGT achieved a limit of detection (LoD) of 138 pg ml^{-1}, which fell between those of the qPCR (13.8 pg ml^{-1}) and the lateral flow immunoassays (LFIAs) (13,800 pg ml^{-1}) used in rapid antigen tests. In contrast, rule-based analysis (relying on a simple classifier) was unable to identify visual artifacts, erroneously perceiving these as clusters and resulting in significant deviations and difficulties in defining the link to the viral load. Auto-filtering of visual artifacts facilitates a dynamic linear correlation at low viral concentration range in the clinical spectra of infection (from 'asymptomatic' to 'severe'), whereas the rule-based algorithm can only ensure spectra above 'moderate'. According to the guidelines of the World Health Organization [60,61], the use of antiviral medications (e.

g., nirmatrelvir and ritonavir) is strongly recommended for moderately and mildly SARS-CoV-2-infected patients, whereas the use of proinflammatory mediators (e.g., IL-6 receptor blockers) is recommended for patients with the moderate or severe levels of infection. Asymptomatic patients with no clinical symptoms or abnormal chest imaging findings are strongly advised to wear face masks [62]. Simple triage and rapid interventions can be facilitated based on the objective quantification of viral loads in subjects' clinical samples, rather than relying on subjective symptoms [10,11,63,64]; this enables its application in point-of-care testing and population-level screening diagnosis to prevent the transmission of pandemic viruses [15].

Transfer learning for the quantification of bioparticles with diverse sizes

Most common viruses have diameters in the range of 20–300 nm and a refractive index similar to that of SiO_2 (~1.5) [16,17,44,45]. Developing new DL models that are virus species-specific, for analyzing viruses of varying sizes requires a large amount of labeled data, which can be challenging and time-consuming to obtain. However, transfer learning—a machine learning technique that repurposes or adapts pre-trained models for different tasks—can significantly reduce the cost and time required to develop new models, by implementing the knowledge gained from solving related problems [65–67]. This approach is particularly helpful when data for new tasks are limited, or training a new model from scratch is computationally expensive or time-consuming. By using only a few additional datasets, the convolutional layers of the CSRNet model, pre-trained using 100-nm-diameter particles, were fine-tuned to adapt for the quantification of virion-mimicking SiO_2 nanoparticles with diameters of 50, 200, and 300 nm, covering many sizes of bioparticles (Fig. 4a). Despite the availability of only a small amount of data, when provided with 120, 251, and 231 images (Supplementary Fig. S18), the transferred models achieved MAEs of 3.59, 2.24, and 2.71, respectively (Fig. 4b). DeepGT demonstrated a modest performance for the 50-nm-diameter NPs, which induce weak light-matter interaction due to their minuscule size. For the 200-nm-diameter NPs, whose size is closer to those mostly trained in the CNN, the MAE was the lowest. During each experiment, the images of the dataset were randomly partitioned into training and testing subsets, and a random item of the training subset (ranging from 20% to 100%) was selected to evaluate the transferability. The relationship between the size of the training dataset and the MAE suggests that increasing the size of the training dataset results in improved accuracy and greater robustness of the transferred model.

Fig. 4c demonstrates the transferable coverage of the fine-tuned model by plotting the sizes of real viruses [68] on a line. Noteworthy, DeepGT is capable of fully quantifying viruses with diameters of 50–300 nm, regardless of the nucleic acid core or the Baltimore classification (see Supplementary Table S4 for details). This size-dependent flexible immunosensing system can be utilized with any antibody suitable for the virus of interest, potentially enabling quick and effective detection of diverse viruses such as Ebola, Zika, and monkeypox viruses [44,45]. The selective immunocapture and quantification of the NPs in the mixture are facilitated by modifying the immobilized antibody on the GT resonator to target specific analytes (Supplementary Fig. S19). Diverse types of particles can be simultaneously quantified using multiple sensing areas, each with immobilized antibodies that are specific to

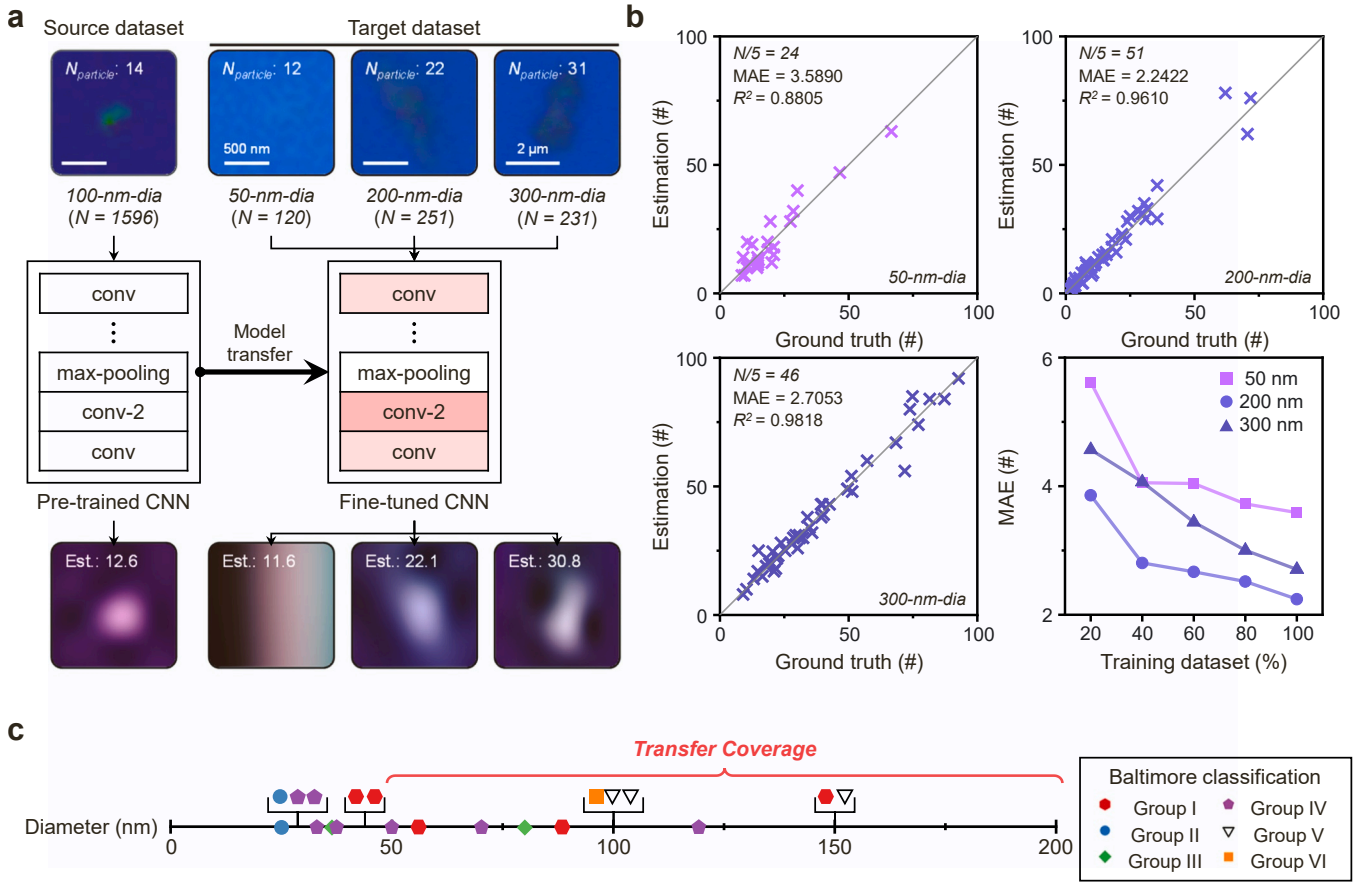

Fig. 4. Transfer learning for different size analytes using fine-tuned CNN. (a) Pre-trained CNN is fine-tuned for transfer learning using the target dataset of nanoparticles with diameters of 50, 200, and 300 nm. (b) Scatter plots of ground truth with respect to estimation and transferability of each size of nanoparticles. (c) Expandability of the fine-tuned CNN to other viruses; *conv-2*: convolution with a dilation rate of two. All scale bars: 1 μm (unless otherwise labeled). The raw SEM and OM images dataset and the annotations are available on the Figshare repository at https://doi.org/10.6084/m9.figshare.c.6468460.v1.

their target analytes. Furthermore, the value of this technology is also intimately intertwined with its capability to address various mutations of a particular virus species [69], which have posed a challenge for conventional testing methods in the recent context of the SARS-CoV-2 pandemic.

Discussion and conclusion

The COVID-19 pandemic overwhelmed our preparedness to screen and diagnose individuals infected with a novel viral pathogen featuring high transmissibility and unanticipated virulence. This has highlighted the importance of decentralized, rapid, accurate, and intuitive diagnostic tests. The gold standard method (i.e., qPCR) provides a definitive result via a long and complex process. However, the qPCR is not widely available in developing countries due to costs and the level of expertise required. In addition, the rapid antigen test kits (e.g., LFIA) faced the drawbacks of restricted sensitivity, low accuracy, and limited quantification when compared to laboratory-based benchtop diagnostics, resulting in a high rate of false negatives. The stratification of patients based on viral load is a crucial step in implementing personalized therapies. The aforementioned tests are inefficient for this purpose. Recent research has led to signal-based breakthroughs through the use of field-effect transistor-based biosensing devices [70], plasmonically enhanced LFIA [71], CRSIPER-Cas12-based LFIA [72], and others [73–79] (Table 1).

In this study, we propose an image-driven quantitative viral sensing framework merging the advantages of GT biosensors and CNNs, which we have named DeepGT. The GT biosensor exploits slow-light effects which result in large color differences between the nanoscale bioparticles and the pristine GT surface. Significantly, the nanosized bioparticles can be detected via a straightforward antibody–antigen reaction, without the need for labeling or amplification. The bright-field micrographs of the GT biosensor facilitate facile immunoassays and intuitive recognition through vision. DeepGT, has a CNN that has been carefully trained using large datasets of experimental SEM and OM images and can accurately infer the quantity of NPs on the biosensor in less than a second. Moreover, the proposed use of auto-filtering and transfer learning facilitates the accurate quantification of various nanoanalytes sized below the microscopy system's minimum diffraction limit in visible light (< 258 nm). Notably, even with limited data availability, the framework can be adjusted to detect bioparticles of different sizes (given that most 'knowledge' is transferred). Such flexibility results in the tremendous potential for testing various nanosized viral pathogens, in the absence of other knowledge other than, their size (and a target protein required for the functionalization of the GT biosensor). DeepGT classifies the bioparticle counts in the concentration of SARS-CoV-2 severity spectrum from 'asymptomatic' to 'severe', thereby facilitating timely and appropriate clinical intervention. For viruses that undergo physical and/or biological changes, additional training datasets are required to enhance the accuracy of quantification. Further, the well-curated datasets introduced in this study can facilitate the data-driven inverse design for nanophotonics and overcome existing challenges such as cluster identification and single-particle reconstruction faster than the conventional method [31,41,80]. DeepGT can be further developed for a more robust quantitation optimized for hazardous bionanoparticles (e.g., emerging pandemic viruses and bacteria) by creating an image repository and storing rich experimental datasets, such as various microscopy techniques [81,82].

Overall, given its sensitivity performance (comparable to the qPCR test) and its affordability (potential price comparable to the LFIA), we believe that DeepGT will serve as the foundation for the next-generation viral diagnostic tools and as a valuable resource for other major medical fields. For example, in cancer diagnosis and treatment, where prompt decision-making is crucial for better patient outcomes, DeepGT can be a potential alternative for detecting cancer biomarkers or immunological responses at the point of care. Additionally, in the realm of drug delivery, the ability to quantify and identify the distribution of nanoparticles provides unbiased information in cancer therapy and facilitates a comprehensive interpretation of research finding [83,84]. We anticipate that using DeepGT for screening and diagnosis in preparation for viruses (which can surpass diffraction limitations) that may emerge in the future, will save time and resources in clinical applications [15,85]. Moreover, DeepGT-generated output datasets may prove valuable in deciphering intricate nanophotonics through a data-driven inverse design methodology, eliminating the need for numerical light-matter interaction modeling or intuition-based iterative parameter exploration [31,41,80]. Beyond nanoscale analytes, we further envision that the GTIP holds immense potential for multi-scale facile visualization/quantification involving various cells and tissues.

Materials and methods

Fabrication of GT resonator

For fabrication, a 100-nm-thick gold thin film (Platypus Technologies, USA) was sonicated, cleaned (sequentially with acetone, isopropanol, and deionized (DI) water), and dried using a nitrogen gun. A 60-nm-thick Ge thin film was deposited on an Au reflector via electron beam evaporation (KVE-E2000, Korea Vacuum Tech, Korea) under high vacuum conditions ($\sim 10^{-6}$ Torr) at a rate of ~1 Å/s. To modulate the

Table 1
Comparison of biosensing techniques for SARS-CoV-2 detection.

Technique	Target analyte	Materials	Equipment	Detection limit	Time	Ref.
RT-PCR	SARS-CoV-2 RNA	DNA Primer, Fluorescent dye	Thermocycler, Fluorescent reader	10 copies μl^{-1}	3 h	[70]
RT-LAMP	SARS-CoV-2 RNA	LAMP primer, Fluorescent dye	Heat bath, Fluorescent reader	50 copies μl^{-1}	1 h	[71]
Colorimetric RT-LAMP	SARS-CoV-2 RNA	LAMP primer, Fluorescent dye	Heat bath, Fluorescent reader	$\sim 10^3$ copies μl^{-1}	30 m	[72]
CRISPR-Cas12 based LFIA	E gene and N gene	LAMP primer, Cas12, LFIA strip	Heat bath, Fluorescent reader	10 copies μl^{-1}	40 m	[69]
Plasmonically enhanced LFIA	N gene	LFIA strip, Fluorescent dye	Fluorescent reader	212 pg ml^{-1}	20 m	[68]
Graphene FET	Spike protein	Graphene-based FET	Parameter analyzer	242 copies ml^{-1}	> 1 m	[67]
SPR	Ig G and Ig M	Biofunctionalized Au sensor	SPR equipment	0.5 μg ml^{-1}	10 m	[73]
LSPR imaging	Pseudovirus	Nanocup array, labeled AuNPs	Fluorescence microscope	125 vp ml^{-1}	12 m	[74]
Thermotropic liquid crystal	SARS-CoV-2 RNA	Cationic surfactant, ssDNA probe	Polarized light microscope	30 fM	20 m	[75]
Colorimetric dark-field	N gene	ASO cappedAuNPs	Hyperspectral-enhanced dark-field microscope	180 pg μl^{-1}	30 m	[76]
DeepGT	*NPs w/ spike protein*	*GT biosensor*	*Optical microscope w/o any accessory*	*138 pg ml^{-1}*	*5 m*	*This work*

Abbreviations: Ref, reference; RT-PCR, reverse transcription polymerase chain reaction; RT-LAMP, reverse transcription loop-mediated isothermal amplification; LFIA, Lateral flow immunoassay; FET, field-effect transistor; SPR, Surface plasmon resonance; Ig, Immunoglobulin; LSPR, Localized Surface plasmon resonance; AuNP, Gold nanoparticle; ASO, Antisense oligonucleotide; GT, Gires-Tournois; w/o, without.

refractive index of the lossy medium, a Ge layer was deposited via glancing angle deposition after being embedded in a customized tilted sample holder at a 70° deposition angle. This process was repeated upside down to form a flat surface at half the target thickness (see Supplementary Fig. S3 for details). Next, a 180-nm-thick SiO_2 passivation layer was deposited using plasma-enhanced chemical vapor deposition (PECVD; System 100, Oxford, USA) with radiofrequency (RF) plasma (170 sccm of SiN_4 gas, 710 sccm of N_2O gas, 20 W, 0.1 Torr, 90 s, 150 °C). To define the sensing area, the top SiO_2 layer was etched to a depth of 100 nm via reactive-ion etching (RIE; PLASMALAB 80 PLUS, Oxford, USA) with a contact-type shadow mask and RF plasma (50 sccm of CF_4 gas, 75 W, 50 mTorr, 3 min). The sensing area was patterned in a square array with a constant spacing between adjacent areas.

Biofunctionalization of GT biosensor

A 5% polyethylene glycol (PEG, Sigma-Aldrich, USA, no. 295906) solution (w/w in 95% tetrahydrofuran) was spin-coated onto the GT resonator at 4000 rpm for 30 s. Subsequently, samples were dried at 80 °C for 7 min, rinsed in pre-made phosphate-buffered saline (PBS; Biosesang Co., Ltd., Korea) for 45 s and Milli-Q water for 15 s, and annealed at 120 °C for 1 min. The PEG-coated surface was immobilized by immersion in 100 μg ml^{-1} IgG (Anti-Spike-RBD-hIgG1, InvivoGen, USA) for 10 min at room temperature (27 °C). To prevent non-specific interactions, this PEG-IgG surface was incubated with 1% bovine serum albumin (BSA) solution (20 mg ml^{-1}) (Biosesang Co., Ltd., Korea) at room temperature for 20 min. The GT biosensor was separated from the chip array wafer using a diamond cutter. A schematic illustration of the biofunctionalization process is shown in Supplementary Fig. S4a.

Viral nanoparticle synthesis

SiO_2 nanospheres with a refractive index of ~1.5 (similar to typical zoonotic viruses) were selected to mimic existing viruses. 1-mg SiO_2 nanoparticles suspended in ethanol were sonicated according to the diameter of the SiO_2 particles (for detailed information, see Supplementary Table S5). The nanoparticles were then dispersed in 50 μl of 1% 3-aminopropyl triethoxysilane (APTES 99%; Sigma-Aldrich, USA, no. 440140) dissolved in 99% ethanol and left overnight at room temperature to cover their surface with amino functional groups. The following day, the mixture was centrifuged at 2000 rpm for 10 min and sequentially immersed in ethanol (0.3 ml) and Milli-Q water (1 ml) three times. Afterward, the particles were submerged in a 10% glutaraldehyde solution (diluted with 50 mM PBS), stored for 3 h, and centrifuged using the same procedures as before. The washed NPs were functionalized using an antigen (50 μg ml^{-1}) injection (Spike-RBD-His, InvivoGen, USA) and then stored overnight at 4 °C. A detailed illustration of the steps is provided in Supplementary Fig. S4b.

Immunoassays on GT biosensor

The viral solutions were diluted in PBS to concentrations ranging from 100 pg ml^{-1} to 500 ng ml^{-1}. A 300-nl volume of each solution was dispensed into each sensing area of the GT biosensor using a gastight micro-syringe (Legato 210, KD Scientific Inc., USA). The circulation and agglomeration of bioparticles in the droplet are driven by hydrodynamic phenomena such as Marangoni flow [46] during the evaporation of the viral solution. Subsequently, the sensor was rinsed with PBS for 30 s and DI water for 10 s to eliminate the non-specific reactions of undesired components in the viral solution (as shown in Supplementary Fig. S4c). The conversion between the mass and number of nanoparticles is illustrated in Supplementary Fig. S4d.

Image acquisition

Optical microscopy (OM) images: The GT biosensor for capturing NPs was mounted onto a motorized scanning stage (SCANplus, Marzhauser Wetzlar, Germany) with a maximum travel speed of 50 mm s^{-1}, to scan the entire sensing area. Optical bright-field images were acquired using a 100 × objectives lens (MPlanFLN, Olympus, Japan) with a CMOS camera (STC-MCCM200U3V, OMRON SENTECH, Japan) connected to a computer. Under a continuous white LED light source, the exposure time required to obtain a single image was 27.5 ms. The imaging field of view (FoV) of a single image was 169 μm × 141.4 μm (2448 × 2048 pixels). The practical FoV for video monitoring observations is

$$\text{FoV} = \frac{\text{Image device size}}{M_{ob} \times M_{VCA}},$$

where Image device size = 8.45 mm × 7.07 mm; M_{ob}: Objective Lens Magnification = 100; and M_{VCA}: projected magnification for video camera adapter (including photo eyepiece) = 0.5.

The whole sensing area (1 mm × 1 mm) was scanned using OM at the maximum travel speed and exposure time for 20 × 20 shots at 50-μm intervals and captured using StCamSWare software (OMRON SENTECH, Japan). The detailed specifications of the optical microscope system are provided in Supplementary Table S6.

Image stitching: The optical micrographs were acquired using a CMOS camera (STC-MCCM200U3V, OMRON SENTECH, Japan) with a maximum frame rate of 35.8 fps; these were consecutively stitched using a customized automatic algorithm in MATLAB to obtain an integrated sensing area image. Considering the travel speed of the motorized stage and the exposure time, the defined sensing area of 1 mm × 1 mm was scanned in a raster pattern in less than 12 s at an optimized speed.

Diffraction limit: The minimum diffraction limit of the microscopy system was determined to be 258 nm, as derived from the following Rayleigh formula:

$$\text{diffraction limit} = 0.61 \times \frac{\lambda}{NA}.$$

Here, λ denotes the wavelength, which is 380 nm for the shortest visible wavelength [86]; *NA* is the numerical aperture of the objective lens, which is 0.9 (see details in Supplementary Table S6).

Scanning electron microscopy (SEM) images: An ultra-high-resolution field emission scanning electron microscope (UHR FE-SEM; Verios 5 UC, ThermoFisher, USA) was used to obtain ground truth images of the NPs at the GIST Central Research Facilities (GCRF). A 3-nm-thick Pt layer was coated on the samples (which consisted of a GT resonator and SiO_2 NPs) using a high-vacuum sputter coater (EM ACE600, Leica, Germany). SEM images were captured at a resolution of 1536 × 1094 pixels and at six magnifications: 20k× , 25k× , 30k× , 50k× , 60k× , and 100k× . The beam current was set to 25 pA or 0.4 nA, and the acceleration voltage was 10 kV or 20 kV, depending on the size of the NPs. To ensure that the NP clusters were located at the center of the images and not cropped out, the samples were carefully placed in the middle of the micrograph.

Transmission electron microscopy (TEM) images: To obtain a cross-sectional view of the slanted Ge nanocolumns, a focused ion beam system (FIB; ETHOS NX5000, HITACHI, Japan) was used to thin the GT biosensor. The prepared specimens were then imaged using a transmission electron microscope (Tecnai G 530 S-Twin, FEI Co., USA) at the GCRF; this was equipped with both FIB and TEM capabilities.

Reproduction of the ground truth density map from SEM images

The data bars of the raw SEM images were trimmed, and the remaining images were converted to grayscale. The raw SEM images lacked sufficient contrast to clearly distinguish the contours of the NPs. To remedy this, neighboring pixels were smoothed using a median filter, and the contrasts of the SEM images were enhanced to increase the recognition rate. The entire image pre-processing was performed in

MATLAB (MathWorks, USA) and is described in Supplementary Fig. S8. A semi-automatic annotator based on the circle Hough Transform (from OpenCV-python) was developed to identify circles and edit the particle position. The annotated positional point of the particle was represented by the delta function $\delta(p - p_i)$ where p_i is the pixel; an annotation with x particles was represented by $H(p) = \sum_{i=1}^{x} \delta(p - p_i)$. To convert the annotation into a continuous density function, a Gaussian kernel G_σ was convolved, resulting in a density represented as $F(p) = H(p) * G_\sigma(p)$.

OM cluster images corresponding to SEM images

The raw OM images were cropped to match the sizes and positions of the clusters in the SEM images, by calculating the required pixels and magnification (see Supplementary Table S7).

Data augmentation

To enrich the training dataset, both the OM and SEM image datasets were augmented using various techniques (including random rotation, flipping, and modification of brightness and hue) within an acceptable range of environmental variations (see Supplementary Fig. S13).

Five-fold cross-validation

The DL model was trained on a dataset consisting of 2336 OM patches and their corresponding SEM images, encompassing particles of diverse sizes (50–300 nm) and 139 hard negative samples. To evaluate the feasibility of the model, we performed a five-fold cross-validation, with four folds used for training and one fold for testing in each iteration. To assess the accuracy of the bioparticle count prediction, we introduced the mean average error (MAE) as a metric:

$$\mathrm{MAE} = \frac{\sum_{i=1}^{n} |y_i - x_i|}{n}.$$

Here, x_i is the forecast value and y_i is the actual value.

Quantitative image analysis using convolutional neural network (CNN)

Training equipment: The training and inference for the GT biosensor dataset were performed on a computer workstation equipped with an Intel Xeon E5–2698 v4 processor at 2.2 GHz (with 20 cores) and an NVIDIA RTX 3090 graphics card with 24 GB of memory.

Training protocol: Our neural network was implemented in the publicly available PyTorch framework using an ADAM optimizer and a learning rate of 0.00001 ($\beta_1 = 0.9$, $\beta_2 = 0.999$); this took one day on a single NVIDIA RTX 3090. The input images were normalized to a zero mean and unit standard deviation to strengthen the learning procedure. The mean and standard deviation of each RGB channel in the OM images were [0.29237282, 0.28632027, 0.43138893] and [0.00953473, 0.01360602, 0.01595942], respectively. The inference time for a single raw OM image was ~3 ms.

Estimation and quantification: The Congested Scene Recognition Network (CSRNet), a model designed for crowd counting, was taken as a baseline model to estimate the number of bioparticles in the OM image cluster. The neural network was composed of two components: a CNN architecture for 2D feature extraction on the front end, and a dilated CNN for the back end; the latter used dilated kernels to achieve larger reception fields and to replace pooling computations.

Transfer learning

Transfer learning is a machine learning technique that involves reusing or modifying a model that has been trained for one task for use on a different—but related—task. The information and characteristics obtained during training on a task can be used to assist the model in learning or improving its performance on related ones. In this study, we fine-tuned a pre-trained DL model to estimate the number of bioparticles of varying sizes, demonstrating its generality and transferability to other types of biological NPs.

Optical calculation

The amplitude and phase of the reflected light from the NP-mounted GT biosensor were calculated using the finite-difference time-domain (FDTD) method with commercial software (FullWAVE, RSoft Design Group, Synopsys, USA). The structure of the NPs was reconstructed in computer-aided design software; the launched light was un-polarized visible light (wavelength: 400–800 nm). For an accurate simulation, all structures (including the GT biosensor) were matched in Euclidean coordinates, and complex parameters such as material dispersions and extinction coefficients were considered. In addition, the simulation conditions were set to a continuous plane wave and a grid size of 5 nm. A custom MATLAB code was developed to identify the effective complex refractive indices (using volume averaging theory) and convert the reflectance to the observed color.

Statistical analyses

All data were analyzed for statistical significance via one-way analysis of variance and Tukey's post-hoc tests, implemented on OriginPro (OriginLab, USA). Statistical significance was determined as $^{*}P < 0.1$, $^{**}P < 0.01$, and $^{***}P < 0.001$. Standard deviation (*SD*) was also used.

Supplementary material related to this article can be found online at doi:10.1016/j.nantod.2023.101968.

CRediT authorship contribution statement

Jiwon Kang: Conceptualization, Methodology, Software, Validation, Formal analysis, Investigation, Resources, Data curation, Writing, Visualization. **Young Jin Yoo:** Conceptualization, Methodology, Validation, Resources, Writing, Visualization, Funding acquisition. **Jin-Hwi Park:** Conceptualization, Methodology, Software, Formal analysis, Investigation, Data curation, Writing. **Joo Hwan Ko:** Methodology, Validation, Resources. **Seungtaek Kim:** Validation, Writing – review & editing, Funding acquisition. **Stefan G. Stanciu:** Validation, Writing – review & editing, Funding acquisition. **Harald A. Stenmark:** Validation, Writing – review & editing. **JinAh Lee:** Validation, Writing – review & editing. **Abdullah Al Mahmud:** Investigation, Data curation. **Hae-Gon Jeon:** Conceptualization, Methodology, Software, Writing, Supervision. **Young Min Song:** Conceptualization, Methodology, Validation, Resources, Writing, Supervision, Project administration, Funding acquisition.

Code availability

The facile quantification and detection of nanoparticles using DeepGT were performed on PyTorch, a library for Python programs that promotes DL approaches. The Python codes for the customized annotator, DL architecture, data augmentation, and transfer learning are available at https://github.com/JinhwiPark/QuantificationBioparticle.

Author contributions

J.K., Y.J.Y, and J.-H.P. contributed equally to this paper.

Declaration of Competing Interest

The authors declare that they have no known competing financial interests or personal relationships that could have appeared to influence the work reported in this paper.

Data availability

I have shared the link to my data/code at the Attach File step.

Acknowledgements

This work was supported by the National Research Foundation of Korea (NRF) grant funded by the Korea government (MSIT) (NRF-2021M3H4A1A04086357, NRF-2022M3H4A1A02046445, NRF-2022M3C1A3081312). This material is partly based upon work supported by the International Technology Center Indo-Pacific (ITC IPAC) and Army Research Office, under Contract No. FA5209-22-P-0162. Y.J.Y. acknowledges support from the NRF (NRF-2021R1C1C2013475). S.K. and J.L. acknowledge support from the NRF (NRF-2017M3A9G6068245, NRF-2022M3A9J1081343, NRF-2023M3A9G6057281). S.G.S. and H.A.S. acknowledge the support of UEFISCDI Grant RO-NO-2019-0601. We thank S. Lim at the GIST Central Research Facility for technical assistance with the SEM.

Appendix A. Supporting information

Supplementary data associated with this article can be found in the online version at doi:10.1016/j.nantod.2023.101968.

References

[1] B.D. Kevadiya, J. Machhi, J. Herskovitz, M.D. Oleynikov, W.R. Blomberg, N. Bajwa, D. Soni, S. Das, M. Hasan, M. Patel, Nat. Mater. 20 (2021) 593–605.
[2] R. Weissleder, H. Lee, J. Ko, M.J. Pittet, Sci. Transl. Med. 12 (2020), eabc1931.
[3] J.H. Soh, H.-M. Chan, J.Y. Ying, Nano Today 30 (2020), 100831.
[4] J. Cheong, H. Yu, C.Y. Lee, J.-U. Lee, H.-J. Choi, J.-H. Lee, H. Lee, J. Cheon, Nat. Biomed. Eng. 4 (2020) 1159–1167.
[5] O. Vandenberg, D. Martiny, O. Rochas, A. van Belkum, Z. Kozlakidis, Nat. Rev. Microbiol. 19 (2021) 171–183.
[6] C. Lucas, P. Wong, J. Klein, T.B. Castro, J. Silva, M. Sundaram, M.K. Ellingson, T. Mao, J.E. Oh, B. Israelow, Nature 584 (2020) 463–469.
[7] Y.D. Gao, M. Ding, X. Dong, Jj Zhang, A. Kursat Azkur, D. Azkur, H. Gan, Yl Sun, W. Fu, W. Li, Allergy 76 (2021) 428–455.
[8] E. Pujadas, F. Chaudhry, R. McBride, F. Richter, S. Zhao, A. Wajnberg, G. Nadkarni, B.S. Glicksberg, J. Houldsworth, C. Cordon-Cardo, Lancet Respir. Med. 8 (2020), e70.
[9] S. Zheng, J. Fan, F. Yu, B. Feng, B. Lou, Q. Zou, G. Xie, S. Lin, R. Wang, X. Yang, BMJ 369 (2020) m1443.
[10] E.S. Savela, A. Viloria Winnett, A.E. Romano, M.K. Porter, N. Shelby, R. Akana, J. Ji, M.M. Cooper, N.W. Schlenker, J.A. Reyes, J. Clin. Microbiol. 60 (2022), e01785-01721.
[11] J. Fajnzylber, J. Regan, K. Coxen, H. Corry, C. Wong, A. Rosenthal, D. Worrall, F. Giguel, A. Piechocka-Trocha, C. Atyeo, Nat. Commun. 11 (2020) 5493.
[12] Y. Wang, H. Kang, X. Liu, Z. Tong, J. Med. Virol. 92 (2020) 538.
[13] I. Smyrlaki, M. Ekman, A. Lentini, N. Rufino de Sousa, N. Papanicolaou, M. Vondracek, J. Aarum, H. Safari, S. Muradrasoli, A.G. Rothfuchs, Nat. Commun. 11 (2020) 4812.
[14] D.B. Larremore, B. Wilder, E. Lester, S. Shehata, J.M. Burke, J.A. Hay, M. Tambe, M.J. Mina, R. Parker, Sci. Adv. 7 (2021), eabd5393.
[15] Z. Habli, S. Saleh, H. Zaraket, M.L. Khraiche, Front. Bioeng. Biotechnol. 8 (2021) 1562.
[16] H. Yao, Y. Song, Y. Chen, N. Wu, J. Xu, C. Sun, J. Zhang, T. Weng, Z. Zhang, Z. Wu, L. Cheng, D. Shi, X. Lu, J. Lei, M. Crispin, Y. Shi, L. Li, S. Li, Cell 183 (2020), 730-738.e713.
[17] L. Ma, S. Zhu, Y. Tian, W. Zhang, S. Wang, C. Chen, L. Wu, X. Yan, Angew. Chem. Int. Ed. 55 (2016) 10239–10243.
[18] J. Jonkman, C.M. Brown, G.D. Wright, K.I. Anderson, A.J. North, Nat. Protoc. 15 (2020) 1585–1611.
[19] J.L. Fan, J.A. Rivera, W. Sun, J. Peterson, H. Haeberle, S. Rubin, N. Ji, Nat. Commun. 11 (2020) 6020.
[20] X. Chen, O. Nadiarynkh, S. Plotnikov, P.J. Campagnola, Nat. Protoc. 7 (2012) 654–669.
[21] C.H. Camp Jr, M.T. Cicerone, Nat. Photonics 9 (2015) 295–305.
[22] J.-H. Rabe, D.A. Sammour, S. Schulz, B. Munteanu, M. Ott, K. Ochs, P. Hohenberger, A. Marx, M. Platten, C.A. Opitz, Sci. Rep. 8 (2018) 1–11.
[23] N. De Jonge, F.M. Ross, Nat. Nanotechnol. 6 (2011) 695–704.
[24] E. Balaur, S. O'Toole, A.J. Spurling, G.B. Mann, B. Yeo, K. Harvey, C. Sadatnajafi, E. Hanssen, J. Orian, K.A. Nugent, Nature 598 (2021) 65–71.
[25] E. Balaur, G.A. Cadenazzi, N. Anthony, A. Spurling, E. Hanssen, J. Orian, K. A. Nugent, B.S. Parker, B. Abbey, Nat. Photonics 15 (2021) 222–229.
[26] G. Zheng, C. Shen, S. Jiang, P. Song, C. Yang, Nat. Rev. Phys. 3 (2021) 207–223.
[27] B. Sharma, R.R. Frontiera, A.-I. Henry, E. Ringe, R.P. Van Duyne, Mater. Today 15 (2012) 16–25.
[28] J. Homola, Anal. Bioanl. Chem. 377 (2003) 528–539.
[29] B. Manifold, E. Thomas, A.T. Francis, A.H. Hill, D. Fu, Biomed. Opt. Express 10 (2019) 3860–3874.
[30] G. Moon, T. Son, H. Lee, D. Kim, Anal. Chem. 91 (2019) 9538–9545.
[31] J.-F. Masson, J.S. Biggins, E. Ringe, Nat. Nanotechnol. (2023) 1–13.
[32] A. Voulodimos, N. Doulamis, A. Doulamis, E. Protopapadakis, Comput. Intell. Neurosci. 2018 (2018).
[33] W. Rawat, Z. Wang, Neural Comput. 29 (2017) 2352–2449.
[34] J. Gu, Z. Wang, J. Kuen, L. Ma, A. Shahroudy, B. Shuai, T. Liu, X. Wang, G. Wang, J. Cai, Pattern Recogn. 77 (2018) 354–377.
[35] J. Jumper, R. Evans, A. Pritzel, T. Green, M. Figurnov, O. Ronneberger, K. Tunyasuvunakool, R. Bates, A. Žídek, A. Potapenko, Nature 596 (2021) 583–589.
[36] D. Schraivogel, T.M. Kuhn, B. Rauscher, M. Rodríguez-Martínez, M. Paulsen, K. Owsley, A. Middlebrook, C. Tischer, B. Ramasz, D. Ordoñez-Rueda, Science 375 (2022) 315–320.
[37] C. Arteta, V. Lempitsky, J.A. Noble, A. Zisserman, Med. Image Comput. Comput. Assist. Inter. 15 (2012) 348–356.
[38] W. Xie, J.A. Noble, A. Zisserman, Comput. Methods Biomech. Biomed. Eng. Imaging Vis. 6 (2018) 283–292.
[39] Y.J. Yoo, J.H. Ko, G.J. Lee, J. Kang, M.S. Kim, S.G. Stanciu, H.-H. Jeong, D.-H. Kim, Y.M. Song, Adv. Mater. 34 (2022), 2110003.
[40] J. Kang, Y.J. Yoo, J.H. Ko, A.A. Mahmud, Y.M. Song, Nanomaterials 13 (2023) 319–330.
[41] S. So, T. Badloe, J. Noh, J. Bravo-Abad, J. Rho, Nanophotonics 9 (2020) 1041–1057.
[42] R.W. Peeling, D.L. Heymann, Y.-Y. Teo, P.J. Garcia, Lancet 399 (2022) 757–768.
[43] X. He, E.H. Lau, P. Wu, X. Deng, J. Wang, X. Hao, Y.C. Lau, J.Y. Wong, Y. Guan, X. Tan, Nat. Med. 26 (2020) 672–675.
[44] H.R. Gelderblom. Medical Microbiology, fourth ed..,, Univ. of Texas Medical Branch at Galveston,, 1996.
[45] J. Louten, Essential Human Virology, Academic Press,, 2016.
[46] J.R. Trantum, M.L. Baglia, Z.E. Eagleton, R.L. Mernaugh, F.R. Haselton, Lab Chip 14 (2014) 315–324.
[47] F. Girard, M. Antoni, K. Sefiane, Langmuir 24 (2008) 9207–9210.
[48] H. Wanzenboeck, P. Roediger, G. Hochleitner, E. Bertagnolli, W. Buehler, J. Vac. Sci. Technol. A 28 (2010) 1413–1420.
[49] B. Zhang, J. Zerubia, J.-C. Olivo-Marin, Appl. Opt. 46 (2007) 1819–1829.
[50] J. Lever, M. Krzywinski, N. Altman, Nat. Methods 13 (2016) 703–705.
[51] T. Fushiki, Stat. Comput. 21 (2011) 137–146.
[52] Y. Li, X. Zhang, D. Chen, Proceedings of the IEEE Conference on Computer Vision and Pattern Recognition 2018, pp. 1091–1100.
[53] K. Simonyan, A. Zisserman, arXiv preprint arXiv:1409.1556 (2014).
[54] Y. Zhang, D. Zhou, S. Chen, S. Gao, Y. Ma, Proceedings of the IEEE Conference on Computer Vision and Pattern Recognition (2016), pp. 589–597.
[55] K. He, X. Zhang, S. Ren, J. Sun, Proceedings of the IEEE Conference on Computer Vision and Pattern Recognition 2016, pp. 770–778.
[56] C. Shorten, T.M. Khoshgoftaar, J. Big Data 6 (2019), 60.
[57] L. Boominathan, S.S. Kruthiventi, R.V. Babu, Proceedings of the 24th ACM International Conference on Multimedia 2016, pp. 640–644.
[58] D.Babu Sam, S. Surya, R.Venkatesh Babu, Proceedings of the IEEE Conference on Computer Vision and Pattern Recognition 2017, pp. 5744–5752.
[59] V.A. Sindagi, V.M. Patel, Proceedings of the IEEE International Conference on Computer Vision 2017, pp. 1861–1870.
[60] A. Agarwal, B. Rochwerg, F. Lamontagne, R.A. Siemieniuk, T. Agoritsas, L. Askie, L. Lytvyn, Y.-S. Leo, H. Macdonald, L. Zeng, BMJ 370 (2020) m3379.
[61] W.H. Organization, World Health Organization (2023).
[62] S. Esposito, N. Principi, C.C. Leung, G.B. Migliori, Eur. Respir. J. 55 (2020), 2001260.
[63] A. Goyal, E.F. Cardozo-Ojeda, J.T. Schiffer, Sci. Adv. 6 (2020), eabc7112.
[64] S. Sanche, T. Cassidy, P. Chu, A.S. Perelson, R.M. Ribeiro, R. Ke, Sci. Rep. 12 (1) (2022) 14.
[65] J. Yosinski, J. Clune, Y. Bengio, H. Lipson, Adv. Neural Inf. Process. Syst. 27 (2014).
[66] C. Tan, F. Sun, T. Kong, W. Zhang, C. Yang, C. Liu, Artificial Neural Networks and Machine Learning–ICANN 2018, Springer,, 2018, pp. 270–279.
[67] F. Zhuang, Z. Qi, K. Duan, D. Xi, Y. Zhu, H. Zhu, H. Xiong, Q. He, Proc. IEEE 109 (2020) 43–76.
[68] M.J. Roossinck, Virus: An illustrated guide to 101 incredible microbes, Princeton University Press,, 2016.
[69] S.S.A. Karim, Q.A. Karim, Lancet 398 (2021) 2126–2128.
[70] G. Seo, G. Lee, M.J. Kim, S.-H. Baek, M. Choi, K.B. Ku, C.-S. Lee, S. Jun, D. Park, H. G. Kim, S.-J. Kim, J.-O. Lee, B.T. Kim, E.C. Park, S.I. Kim, ACS Nano 14 (2020) 5135–5142.
[71] R. Gupta, P. Gupta, S. Wang, A. Melnykov, Q. Jiang, A. Seth, Z. Wang, J. J. Morrissey, I. George, S. Gandra, P. Sinha, G.A. Storch, B.A. Parikh, G.M. Genin, S. Singamaneni, Nat. Biomed. Eng. (2023), https://doi.org/10.1038/s41551-022-01001-1.
[72] J.P. Broughton, X. Deng, G. Yu, C.L. Fasching, V. Servellita, J. Singh, X. Miao, J. A. Streithorst, A. Granados, A. Sotomayor-Gonzalez, Nat. Biotechnol. 38 (2020) 870–874.
[73] C.B. Vogels, A.F. Brito, A.L. Wyllie, J.R. Fauver, I.M. Ott, C.C. Kalinich, M. E. Petrone, A. Casanovas-Massana, M. Catherine Muenker, A.J. Moore, Nat. Microbiol. 5 (2020) 1299–1305.
[74] W.E. Huang, B. Lim, C.C. Hsu, D. Xiong, W. Wu, Y. Yu, H. Jia, Y. Wang, Y. Zeng, M. Ji, Microb. Biotechnol. 13 (2020) 950–961.

[75] V.L. Dao Thi, K. Herbst, K. Boerner, M. Meurer, L.P. Kremer, D. Kirrmaier, A. Freistaedter, D. Papagiannidis, C. Galmozzi, M.L. Stanifer, Sci. Transl. Med. 12 (2020), eabc7075.
[76] C.R. Basso, C.D. Malossi, A. Haisi, V. de Albuquerque Pedrosa, A.N. Barbosa, R. T. Grotto, J.P.A. Junior, Anal. Methods 13 (2021) 3297–3306.
[77] J. Liang, W. Zhang, Y. Qin, Y. Li, G.L. Liu, W. Hu, Biosensors 12 (2022) 173.
[78] Y. Xu, A.M. Rather, S. Song, J.-C. Fang, R.L. Dupont, U.I. Kara, Y. Chang, J. A. Paulson, R. Qin, X. Bao, Cell Rep. Phys. Sci. 1 (2020), 100276.
[79] P. Moitra, M. Alafeef, K. Dighe, M.B. Frieman, D. Pan, ACS nano 14 (2020) 7617–7627.
[80] S. Molesky, Z. Lin, A.Y. Piggott, W. Jin, J. Vucković, A.W. Rodriguez, Nat. Photonics 12 (2018) 659–670.
[81] E. Williams, J. Moore, S.W. Li, G. Rustici, A. Tarkowska, A. Chessel, S. Leo, B. Antal, R.K. Ferguson, U. Sarkans, Nat. Methods 14 (2017) 775–781.
[82] M. Lelek, M.T. Gyparaki, G. Beliu, F. Schueder, J. Griffié, S. Manley, R. Jungmann, M. Sauer, M. Lakadamyali, C. Zimmer, Nat. Rev. Methods Prim. 1 (2021) 39.
[83] M.J. Mitchell, M.M. Billingsley, R.M. Haley, M.E. Wechsler, N.A. Peppas, R. Langer, Nat. Rev. Drug Discov. 20 (2021) 101–124.
[84] A.C. Anselmo, S. Mitragotri, Bioeng. Transl. Med. 4 (2019), e10143.
[85] T.R. Mercer, M. Salit, Nat. Rev. Genet. 22 (2021) 415–426.
[86] D. Sliney, Eye 30 (2016) 222–229.